Supplementary Material

Hydraulic fracture during epithelial stretching

Laura Casares, Romaric Vincent, Dobryna Zalvidea, Noelia Campillo, Daniel Navajas, Marino Arroyo, and Xavier Trepat

This document contains:

- Supplementary Video legends 1 to 7..... 2
- Supplementary Figures 1 to 17 3
- Supplementary Methods 16
- Supplementary Notes 1 to 3 19
- Supplementary References 35

Supplementary Video legends

Supplementary Video 1| Time-lapse imaging (phase-contrast) of a MDCK cluster before, during, and after a 10 min pulse of 10% biaxial strain. Epithelial clusters are 80 μm in diameter.

Supplementary Video 2| Time-lapse imaging (epifluorescence) of a LifeAct-GFP MDCK cluster before, during, and after a 10 min pulse of 10% biaxial strain. Epithelial clusters are 80 μm in diameter.

Supplementary Video 3| Time-lapse imaging (epifluorescence) of a MDCK cluster expressing LifeAct-GFP (left) and E-cad-RFP (right) before, during, and after a 10 min pulse of 10% biaxial strain. Initial gaps in LifeAct-GFP images are untransfected cells. Epithelial clusters are 80 μm in diameter.

Supplementary Video 4| Finite Element simulations of the solvent pressure and deformation of the gel during the stretch-unstretch maneuver in the presence of an impermeable disc-like barrier.

Supplementary Video 5| Time-lapse imaging (epifluorescence) of a LifeAct-GFP MDCK cluster of 200 μm in diameter (left) and 80 μm in diameter (right) before, during and after a 10% biaxial strain.

Supplementary Video 6| Time-lapse imaging (epifluorescence) of a LifeAct-GFP MDCK cluster during two consecutive 10 min pulses of 10% biaxial strain (spaced 30 min). (left) first pulse; (right) second pulse. Epithelial clusters are 80 μm in diameter.

Supplementary Video 7| Effect of blebbistatin on epithelial fracture and healing. Left panel: Time-lapse imaging (epifluorescence) of a LifeAct-Ruby MDCK cluster during a stretch/unstretch maneuver (10 min pulses of 10% biaxial strain). Right panel: the same cell cluster subjected to the same stretch/unstretch maneuver after incubation with Blebbistatin (30 min). Epithelial clusters are 80 μm in diameter.

Supplementary Figures

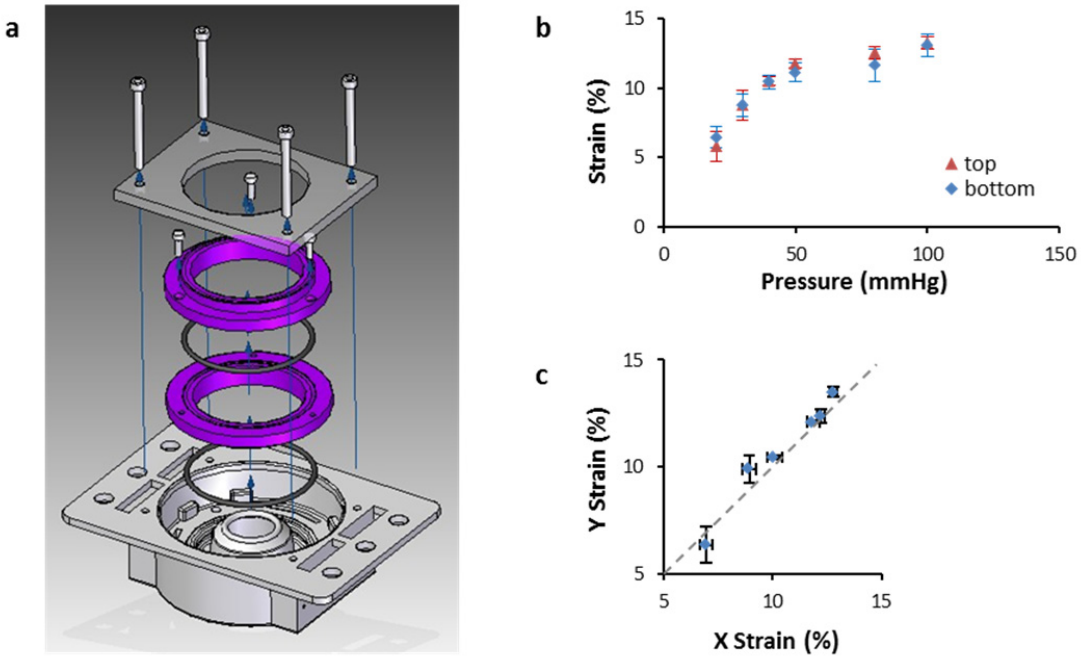

Supplementary Figure 1| Stretching device and strain calibration. a, 3D scheme of the stretching setup. A stretchable PDMS membrane (not shown) is clamped between two Teflon rings (purple) and placed on top of a circular loading post. Application of vacuum to the outer annular region of the membrane causes uniform biaxial strain. **b**, Strain of the top and bottom surfaces of the PAA hydrogel as a function of the applied vacuum (n=2 membranes). **c**, Strain in Y-direction versus strain in X-direction measured on the top surface of a PAA hydrogel. Dashed line represents the identity line (equibiaxial strain). For calibration, each pressure step was applied in random order from the relaxed state. Error bars show SEM.

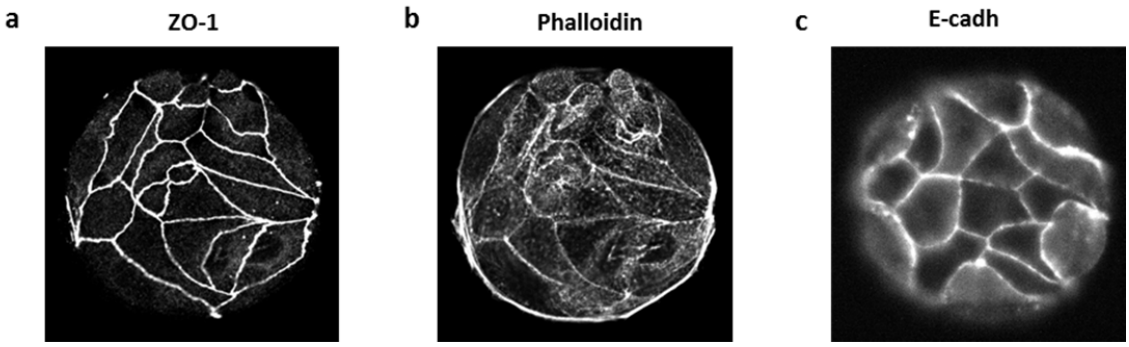

Supplementary Figure 2| Epithelial clusters display features of a polarized epithelium. a,b, ZO-1 (**a**) and phalloidin (**b**) immunofluorescence micrographs of a MDCK cluster on a PAA hydrogel. **c,** Live fluorescence image of a MDCK cluster expressing E-cadh-RFP on a PAA hydrogel. Epithelial clusters are 80 μm in diameter.

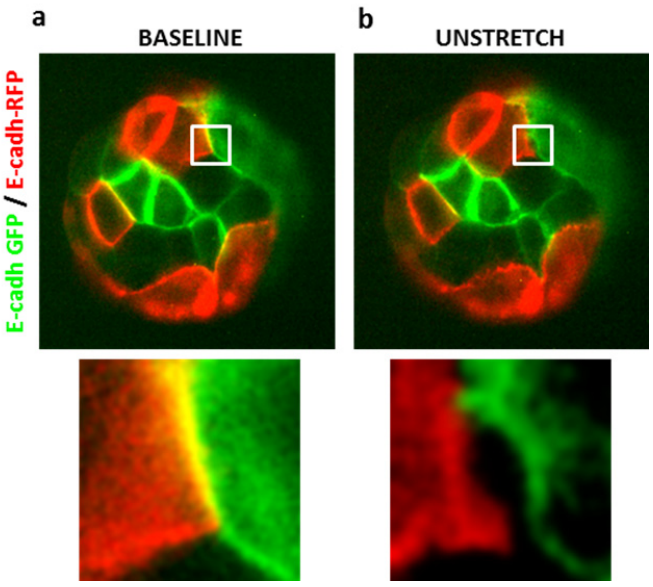

Supplementary Figure 3| Disruption of adherens junctions in a mosaic cluster of E-cadherin-GFP and E-cadherin-RFP. a,b, Mosaic patterns immediately before (a) and after (b) a 10 min pulse of 10% biaxial strain. The bottom row is a magnified view of the region highlighted in the upper row. Epithelial clusters are 80 μm in diameter.

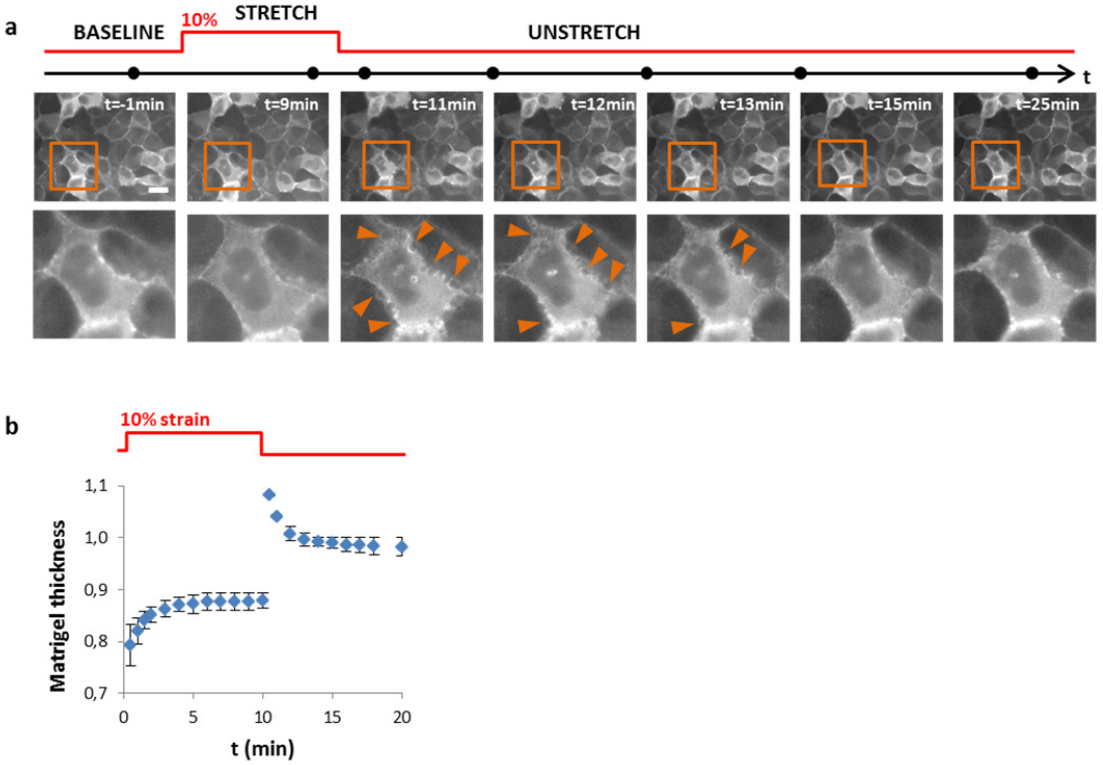

Supplementary Figure 4| Hydraulic fracture in epithelial cells on Matrigel. a, Live fluorescence images of MDCK cells expressing LifeAct-GFP on Matrigel before, during and after a 10 min pulse of 10% biaxial strain. The acquisition time of each snap shot is marked by a black dot on the time axis. The bottom row is a zoom of the region highlighted in the upper row. Arrowheads point at cracks after stretch cessation. **b**, Matrigel thickness during and after a 10 min pulse of 10% biaxial stretch (normalized to baseline thickness). Error bars show SEM of n=2 samples. Scale bar, 20 µm.

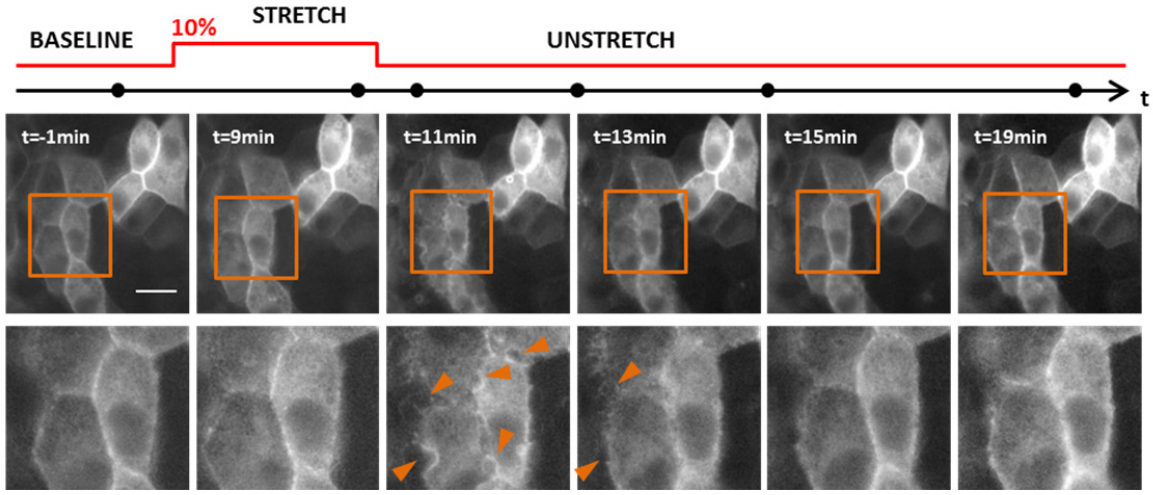

Supplementary Figure 5| Hydraulic fracture in epithelial cells on decellularized tissue from porcine trachea. Live fluorescence images of MDCK cells expressing LifeAct-GFP on decellularized tissue from porcine trachea before, during and after a 10 min pulse of 10% biaxial strain. The acquisition time of each snap shot is marked by a black dot on the time axis. The bottom row is a zoom of the region highlighted in the upper row. Arrowheads point at cracks after stretch cessation. Scale bar, 20 μm.

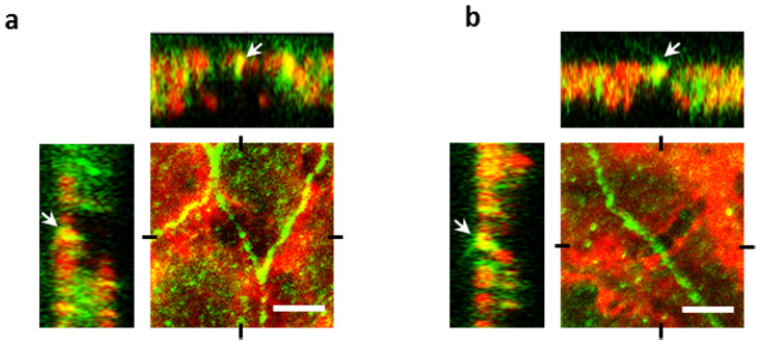

Supplementary Figure 6| a,b, Confocal x-y, x-z and y-z sections of cracks. Cells were fixed immediately after stretch cessation and stained for F-actin (red, phalloidin) and ZO-1 (green, maximum intensity projection). White arrows point at tight junctions on top of the cracks. Images were obtained with a confocal microscope Zeiss LSM-780 with a 63x oil 1.4NA lens. Scale bar, 5µm.

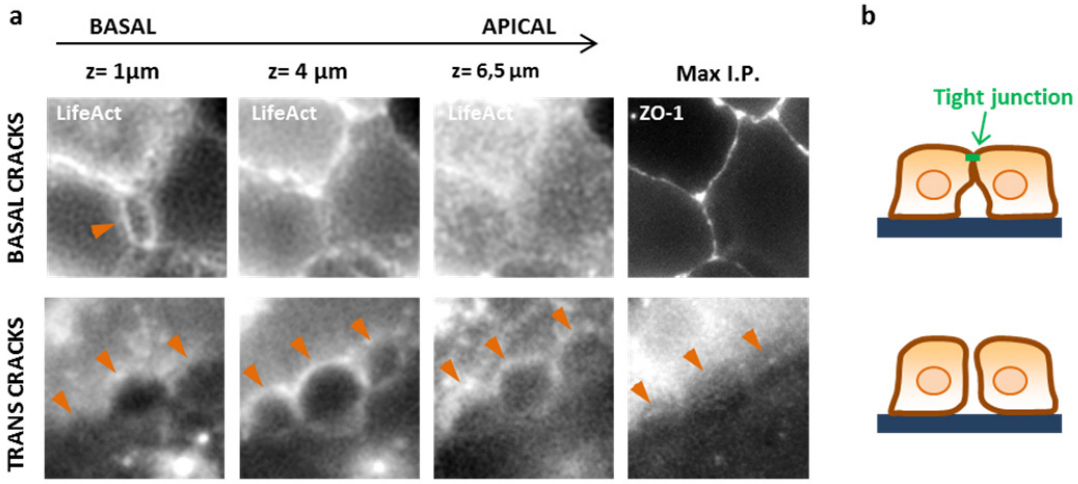

Supplementary Figure 7| Crack localization: basal cracks versus trans cracks. a, Z-stacks in LifeAct-Ruby/ZO-1-GFP cells illustrating two distinct types of cracks upon stretching: basal cracks, which were largely predominant (top), and trans cracks, which were rare (bottom). The first three columns show LifeAct in three different planes. The last column shows a maximum intensity projection of ZO-1-GFP. Arrowheads point at cracks after stretch cessation. **b**, Drawings illustrating the two types of cracks.

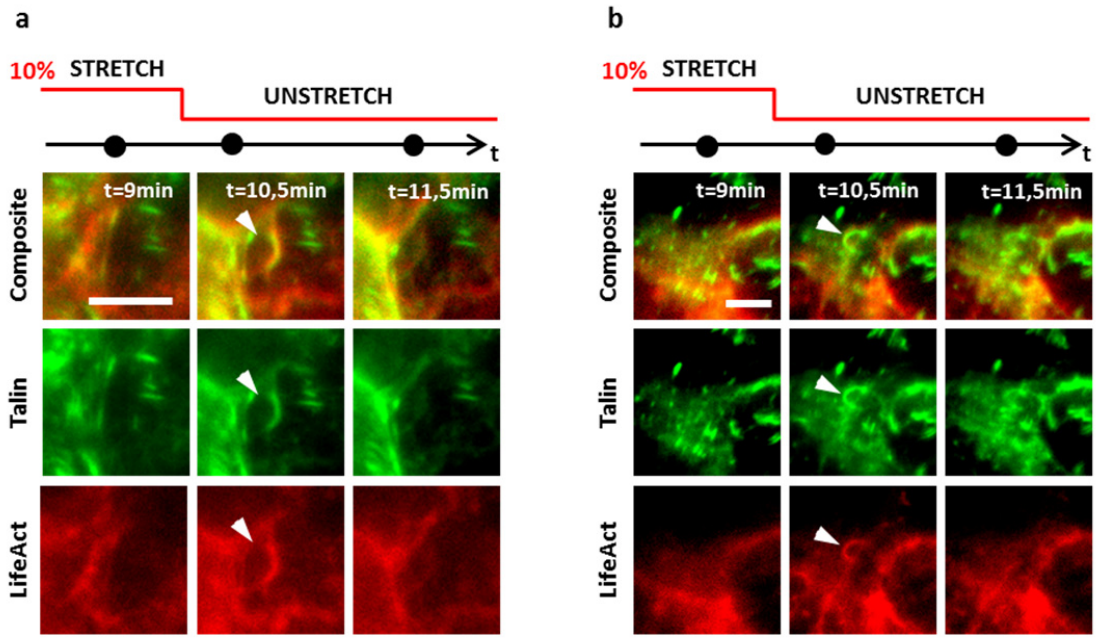

Supplementary Figure 8| Focal adhesion remodeling during crack formation. a,b, Two representative examples of talin remodeling at the basal plane of epithelial cracks. Time lapse evolution of magnified regions inside a pattern expressing LifeAct-Ruby (bottom), talin-GFP (middle) and the corresponding merged image (top), during and after a 10 min pulse of 10% biaxial stretch. The acquisition time of each snap shot is marked by a black dot on the time axis. Arrowheads point at cracks after stretch cessation. Scale bar, 5 μm.

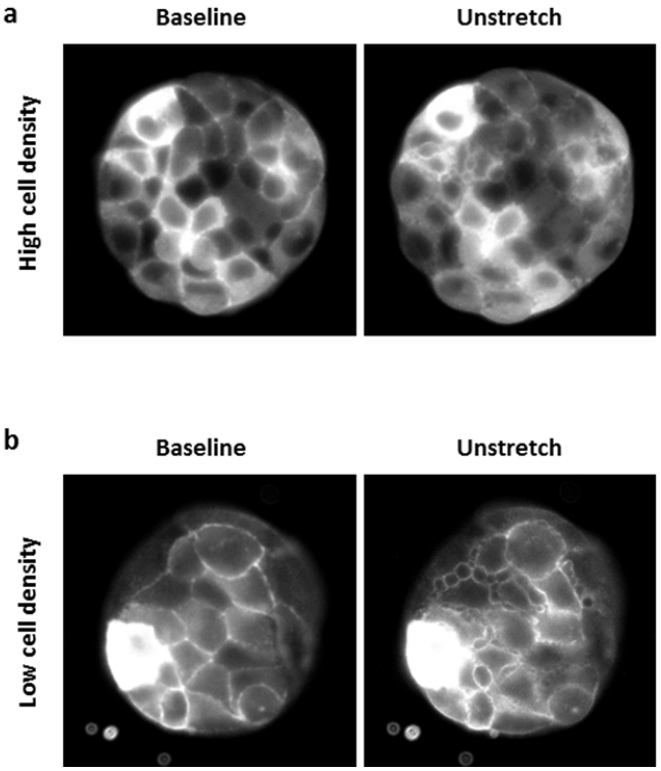

Supplementary Figure 9| Epithelial fracture in clusters with different cell density. a,b, Live fluorescent images of MDCK clusters expressing LifeAct-GFP at high cell density (a) and low cell density (b) before and after a 10 min pulse of 10% biaxial strain. Crack area was highest in low density clusters (see Fig. 1h). Epithelial clusters are 80 μm in diameter.

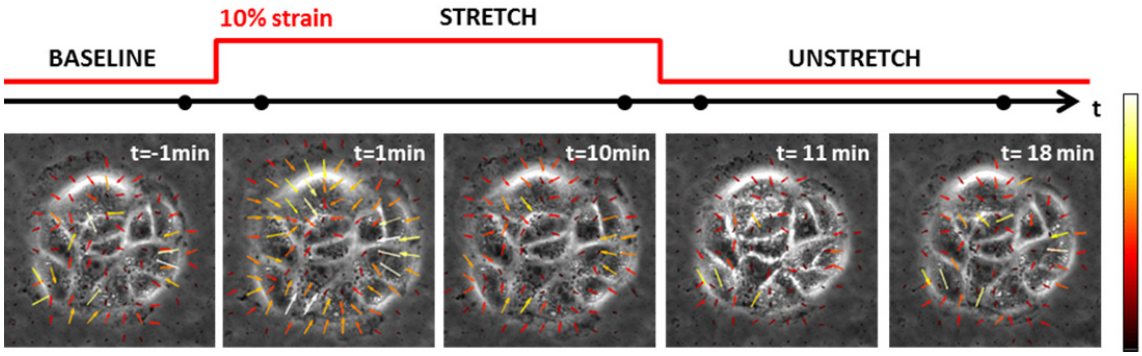

Supplementary Figure 10| Epithelial traction forces during stretch/unstretch maneuvers. Traction vectors showing epithelial tractions of a cluster of MDCK cells on 12 kPa PAA hydrogels before, during, and after a 10 min pulse of 10% biaxial stretch. The acquisition time of each snap shot is marked by a black dot on the time axis. Epithelial clusters are 80 μm in diameter.

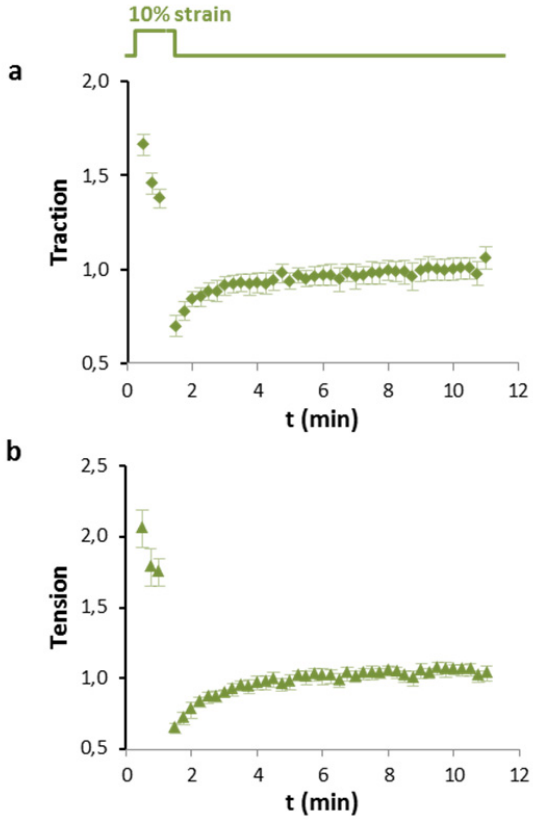

Supplementary Figure 11| Epithelial traction forces during stretch maneuvers. Total traction force and tension during and after a 1 min 10% stretch pulse (both normalized to baseline levels). Error bars represent the standard error of n=6 experiments.

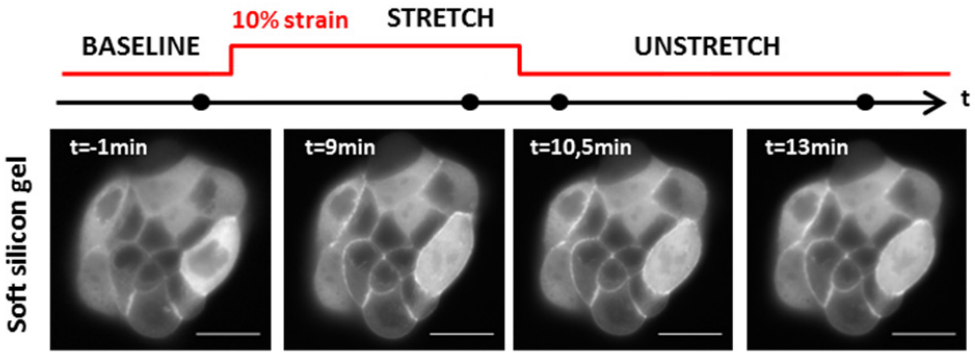

Supplementary Figure 12| Interfacial cracks are absent on soft silicone gel substrates. Live fluorescence images of a MDCK cluster expressing LifeAct-GFP on a collagen coated soft silicone gel before, during and after a 10 min pulse of 10% biaxial strain. The acquisition time of each snap shot is marked by a black dot on the time axis. Scale bar, 20 µm.

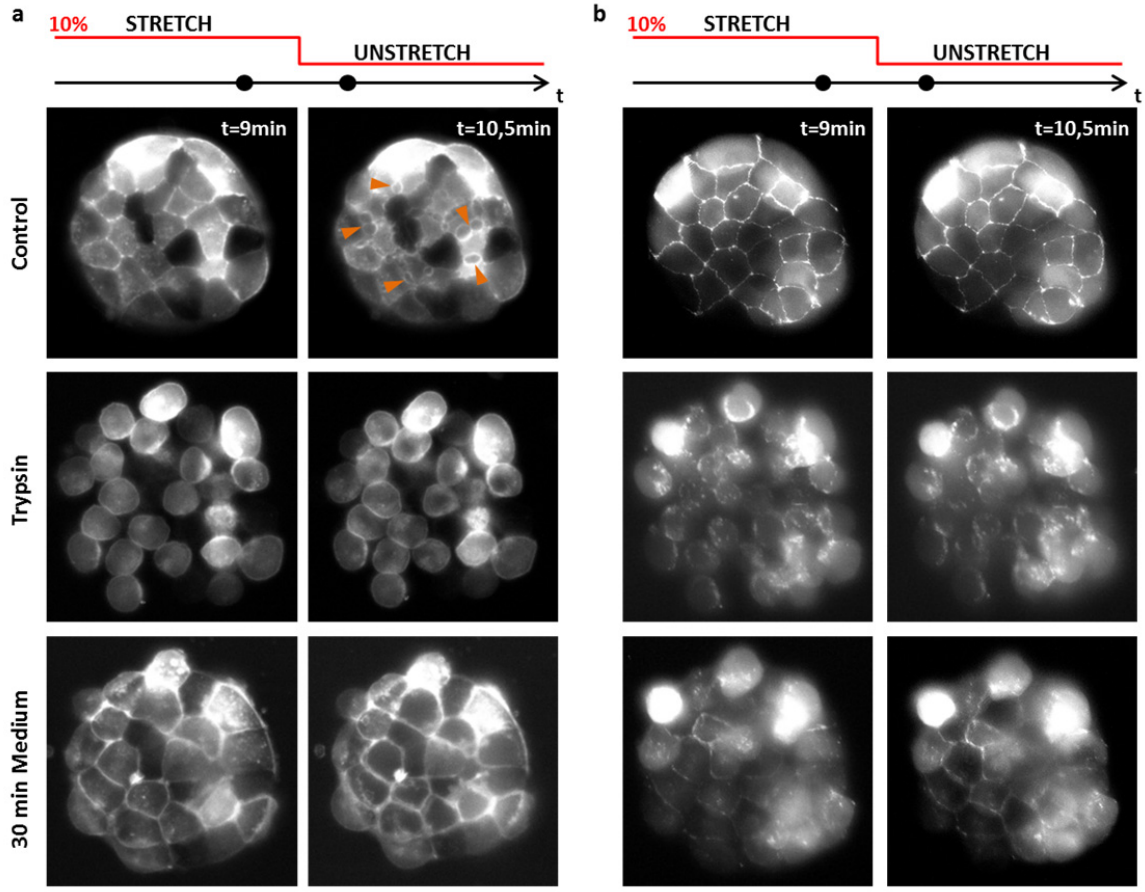

Supplementary Figure 13| Crack formation in clusters with different permeabilities. a,b, Live fluorescent images of MDCK clusters expressing LifeAct-Ruby (a) and ZO-1-GFP (b) during and after 10 min pulses of 10% biaxial strain. Cells were first subjected to a stretch/unstretch pulse in regular culture medium. Upon stretch cessation, cracks appeared in most cell-cell junctions (first row). After crack sealing, we replaced the medium with trypsin 0.5X for 5 min. As expected, cells rounded up and ZO-1 became cytoplasmic. We then applied a second stretch/unstretch pulse and no cracks were observed (second row). Finally, we replaced trypsin with fresh cell culture medium and cells re-adhered on the substrate. After 30 minutes, cells formed a confluent monolayer, actin localized at the cell cortex, but ZO-1 remained partly cytoplasmic, indicating leakiness. Upon applying a third stretch/unstretch pulse, no cracks were visible. The acquisition time of each snap shot is marked by a black dot on the time axis. Arrowheads point at cracks. Epithelial clusters are 80 μm in diameter.

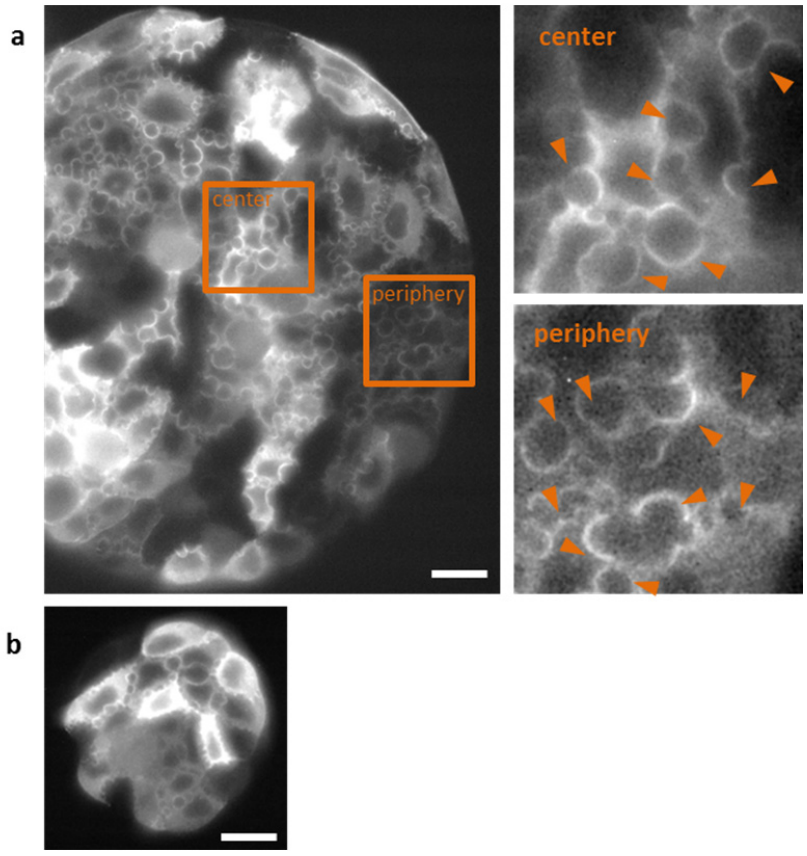

Supplementary Figure 14| Epithelial fracture is independent of cluster size. a, Live fluorescent image of MDCK cells expressing LifeAct-GFP after stretch cessation in a 200 µm cluster (10% biaxial strain). Orange squared boxes are magnified in right panels to highlight fracture in the center versus periphery of the cluster. Arrowheads point to a subset of cracks. **b**, Live fluorescent image of MDCK cells expressing LifeAct-GFP after stretch cessation in a 80 µm cluster (10% biaxial strain). Scale bar, 20 µm. See also Supplementary Video 5.

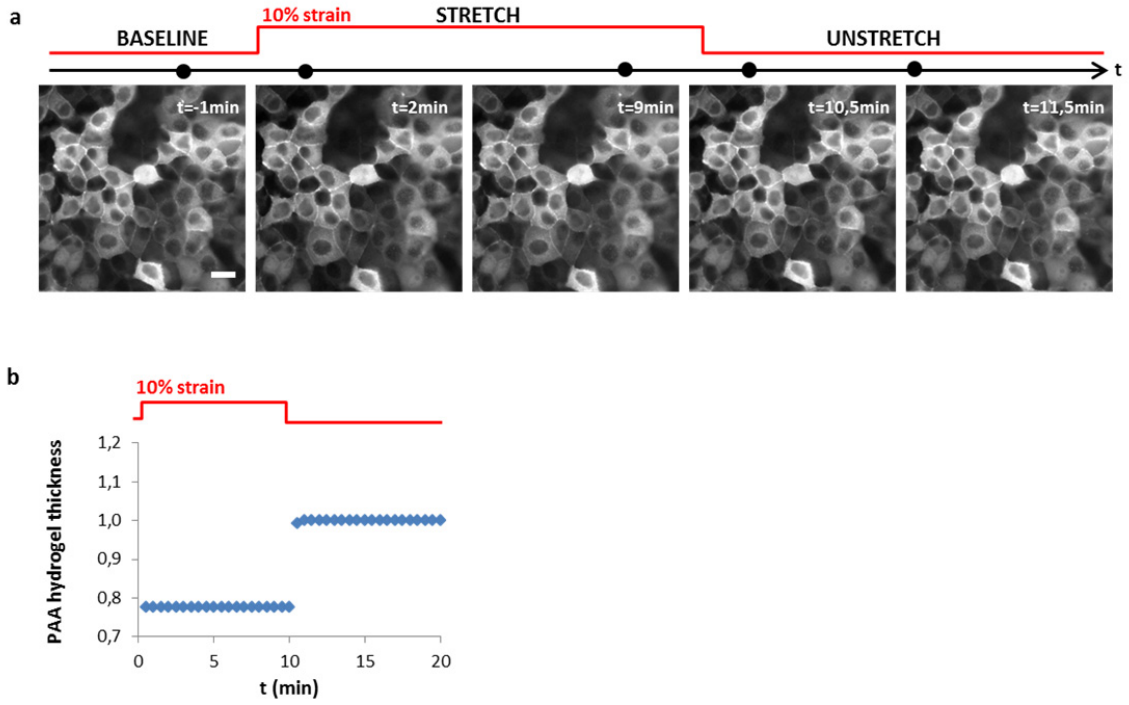

Supplementary Figure 15| Absence of epithelial fracture in a continuous epithelial monolayer. a, Live fluorescence images of a continuous MDCK cell monolayer expressing LifeAct-GFP before, during and after a 10 min pulse of 10% biaxial strain. The acquisition time of each snap shot is marked by a black dot on the time axis. **b**, PAA hydrogel thickness during and after a 10 min pulse of 10% biaxial stretch (normalized to baseline thickness). Scale bar, 20 μm.

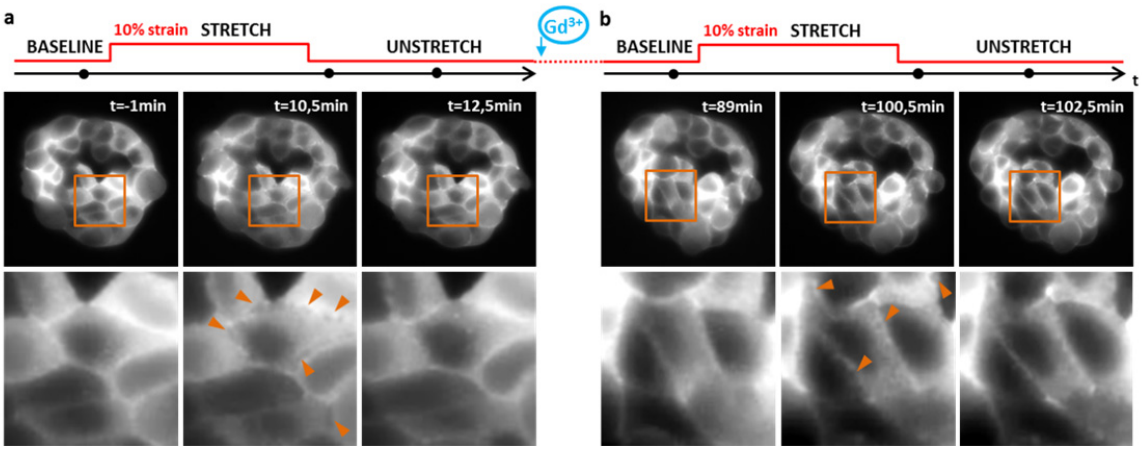

Supplementary Figure 16| Epithelial fracture in clusters treated with Gadolinium. a,b, Live fluorescent images of a MDCK cluster expressing LifeAct-GFP before and after two consecutive 10 min pulses of 10% biaxial strain. Cells were first stretched in control medium (a). Then cells were incubated in 100µM Gd^{3+} for 1 h and 200µM Gd^{3+} for 30 min before applying a second stretch pulse (b). The acquisition time of each snap shot is marked by a black dot on the time axis. The bottom row is a zoom of the region highlighted in the upper row. Arrowheads point at cracks. Epithelial clusters are 80 µm in diameter.

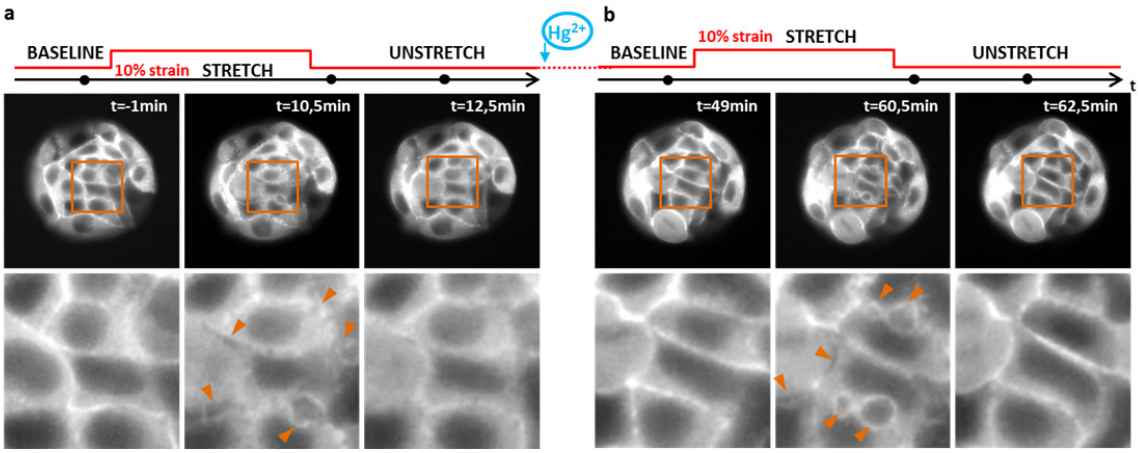

Supplementary Figure 17| Epithelial fracture in clusters treated with HgCl. a,b, Live fluorescent images of a MDCK cluster expressing LifeAct-GFP before and after two consecutive 10 min pulses of 10% biaxial strain. Cells were first stretched in control medium (a). Then cells were incubated in 0.2µM Hg^{2+} for 30 min before applying a second stretch pulse (b). The acquisition time of each snap shot is marked by a black dot on the time axis. The bottom row is a zoom of the region highlighted in the upper row. Arrowheads point at cracks. Epithelial clusters are 80 µm in diameter.

Supplementary methods

MDCK cell culture. Madin Darby canine kidney (MDCK) strain II cells and stable cell lines expressing LifeAct-GFP, LifeAct-Ruby, E-cadherin-RFP, E-cadherin-GFP or ZO-1-GFP were cultured in minimum essential media with Earle's Salts and l-glutamine (Gibco) supplemented with 10% fetal bovine serum (FBS; Gibco), 100 μg/ml penicillin and 100 μg/ ml streptomycin. Selection antibiotic geneticin was added at 0.5 mg/ml to LifeAct stable cell lines. MDCK II expressing both MHC-GFP and LifeAct-Ruby were cultured in Dulbecco's Modified Eagle Medium supplemented with Glutamax (Gibco), 10% fetal bovine serum (FBS; Gibco), 100 μg/ml penicillin and 100 μg/ ml streptomycin. Cells were maintained at 37 ºC in a humidified atmosphere with 5% CO_2. During experiments, cells were serum deprived and supplemented with 25 mM Hepes.

Transfection. To image the plasma membrane / talin during stretch experiments, CellLight plasma membrane-GFP / CellLight talin-GFP (Lifetechnologies) was transfected to LifeAct-Ruby MDCK cells. Two hours after cell seeding and 16 h prior to the experiment, 2 μl of CellLight were added to the medium. Stable cell lines expressing either E-cadherin-RFP or ZO-1-GFP were transfected with LifeAct-GFP or LifeAct-Ruby plasmids respectively, using Neon TM Transfection system (Invitrogen) two days prior to the experiments.

Pharmacological interventions. The following pharmacological interventions were used to perturb the actomyosin cytoskeleton: blebbistatin (80 μM, 30 min incubation), Y-27632 and ML-7 (30 μM and 60 μM respectively, 30 min incubation) and CK-666 (50 μM, 1 h incubation). To perturb tissue permeability cells were treated with trypsin 0.5x after several washes with PBS. To perturb stretch-activated-channels cells were treated with Gadolinium chloride 100-200 μM for 60-90 min (from a stock solution 10 mM in water). To block water transport through aquaporins 2 and 3 cells were treated with 0.2 μM $HgCl_2$ for 30 min (from a stock solution 10 μM in water).

PDMS patterning membranes. Polydimethylsiloxane (PDMS) membranes for micropatterning were fabricated according to procedures described previously[1-3]. Briefly, SU8-50 masters containing cylinders of 80 μm or 200 μm in diameter were raised using

conventional photolithography. Uncured PDMS was spin-coated on the masters to a thickness lower than the height of the SU8 feature (35 μm) and cured for 2 h at 65 °C. A thick border of PDMS was added at the edges of the membranes for handling purposes. PDMS was then peeled off from the master and kept in ethanol at 4 °C until use.

Soft silicone gel. Soft elastomeric silicone gels were prepared using a protocol based on previous publications[4-6]. Briefly, silicone elastomer was synthesized by mixing a 1:1 weight ratio of CY52-276A and CY52-276B (Dow Corning Toray). After degassing, the gel was cured at 80 ºC for 2 h on treated stretchable PDMS membranes.

Time-lapse microscopy. Multidimensional acquisition for traction force measurements was performed at 20× on an automated inverted microscope (Nikon Eclipse Ti) equipped with temperature control, using MetaMorph (Universal Imaging) software. High magnification images (60×, 1.0 NA, dipping lens) were obtained on an upright microscope (Nikon Eclipse Ni) equipped with temperature control using either NIS Elements AR 4.10.00 (Nikon) software or MetaMorph (Universal Imaging) software.

Crack area measurements. Image analysis of cracks was performed using ImageJ. The contour of each crack was manually determined at a z-plane approximately 5 μm above the basal plane (except for crack sealing experiments where several z-planes were considered).

Hydrogel thickness measurements. The thickness of PAA hydrogels or matrigel was determined by measuring the z-distance between fluorescent beads at the top and bottom planes of the hydrogels every 0.5-1 min.

Immunostaining. To assess the cohesiveness and polarity of the epithelium (Supplementary Fig. 2), cells were patterned on 12 kPa PAA hydrogels adhered on glass substrates. MDCK cells were washed with PBS, fixed with 4% paraformaldehyde in PBS for 10 min at room temperature and permeabilized in 0.25% Triton X100 in PBS for 20 min at room temperature. Cells were blocked in 10% FBS in PBS for 1 h prior to incubation for 1.5 h with primary antibody (1:1000 dilution for ZO-1 in blocking solution). Secondary antibody was added at 1:200 dilution (with 1:1000 of Phalloidin) and incubated for 1.5 h. To assess the shape of the cracks (Fig. 1f,g, Supplementary Fig. 6), cells were patterned on

12kPa PAA hydrogels adhered on PDMS stretchable membranes. Immediately after stretch cessation cells were fixed with 8% paraformaldehyde in PBS (without previous washes) for 10 min followed by permeabilization and blocking and antibody incubation as described above. All cells were then washed and mounted in Mowiol reagent. Unless noted otherwise, images were acquired with a Nikon C1Si confocal microscope using a 60× 1,4NA lens.

Supplementary Note 1: Hydrogel theory and finite element calculations

1. Ideal elastomeric hydrogel behavior: theory

An elastomeric hydrogel is a network of cross-linked long polymer chains swollen with a solvent. The small molecules of the solvent can migrate in, out, and move within the polymeric gel. A dry gel placed in a solvent medium will attract solvent to increase the mixing entropy by diluting the chain segments, which can be viewed as osmolites. However, as the gel swells, the polymer chains stretch and decrease their entropy, reaching eventually an equilibrium swelling ratio. External mechanical stretching of the gel is a bias on the network free energy, further driving solvent influx (swelling). Conversely, mechanical compression increases the chemical potential of the solvent inside the gel, driving efflux (de-swelling).

Ideal elastomeric gels, such as polyacrylamide (PAA) hydrogels, are very well described by a recent nonlinear theory.[7,8,9] The ideal behavior is complicated if the solvent contains ions and the polymer is a polyelectrolyte.[10] Here, we deal with a neutral polyacrylamide gel, which has been shown to be quite insensitive to ionic strength within the ranges of the phosphate buffered saline (PBS) solution used here.[11] Therefore, our polyacrylamide-PBS gels can be expected to behave like an ideal elastomeric gel.

We describe next the theory coupling the large deformation of the gel with the mass transport of the solvent.[7] Adopting a Lagrangian description of deformation, we suppose that the gel occupies a region Ω_0 in its reference dry state. The coordinates $\boldsymbol{X}$ in this reference state label material particles. The particle $\boldsymbol{X}$ is placed at position $\boldsymbol{x}(\boldsymbol{X}, t)$ after deformation (possibly involving swelling) in time t. The deformation gradient measuring local strain is then $F_{iI}(\boldsymbol{X}, t) = \partial x_i / \partial X_I(\boldsymbol{X}, t)$. In the total Lagrangian description of the gel, all quantities are referred to the fixed reference state. For instance, $C(\boldsymbol{X}, t)$ denotes the molar concentration of solvent molecules per unit reference volume of a material particle that was in position $\boldsymbol{X}$ at $t = 0$.

Following Flory and Huggins, the free energy per unit volume of dry polymer can be written in terms of the deformation gradient and the chemical potential of the solvent $\mu(\boldsymbol{X}, t)$ as[12]

$$W(\boldsymbol{F}, \mu) = \frac{NkT}{2}\left[\mathrm{tr}\,(\boldsymbol{F}^T\boldsymbol{F}) - 3 - 2\log\ J\right] + \frac{kT}{v}f(J) - \frac{\mu}{v}(J-1), \tag{1}$$

where N is the number of polymer chains per unit reference volume, $J = \det \boldsymbol{F}$ is the Jacobian determinant measuring volume changes relative to the dry reference state, k is the Boltzmann constant, T the temperature, and v is the molar volume of solvent. The term multiplied by N is the network free energy, while the term involving

$$f(J) = (J-1)\log\frac{J-1}{J} + \chi\frac{J-1}{J}. \tag{2}$$

is the mixing free energy, consisting of an entropic and an enthalpic term; $\chi > 0$ provides a negative enthalpic affinity between the polymer and the solvent, and when $\chi < 0.5$, this free energy always favors increasing the amount of solvent molecules per unit volume of dry polymer. The fact that volume changes of the gel can only occur due to solvent migration is expressed in the theory by the molecular incompressibility condition, $1 + Cv = J$, which

allows us to compute the molar concentration of solvent molecules per unit reference volume as $C = -\partial W/\partial\mu = (1 - J)/v$. This form of the free energy, as compared to an alternative form in terms of $\boldsymbol{F}$ and C,[7] is more convenient for the finite element implementation of the theory.[12]

Conservation of solvent molecules, in the absence of solvent sources, can be expressed as

$$\frac{\partial C}{\partial t} = -\nabla_0 \cdot \boldsymbol{J} \tag{3}$$

where $\boldsymbol{J}$ is the nominal flux of solvent (per unit undeformed area) and naught in ∇_0 indicates that derivatives are taken with respect to material coordinates $\boldsymbol{X}$.

The diffusive flux of solvent molecules adopts the classical form

$$\boldsymbol{j} = -\frac{cD}{kT}\nabla\mu, \tag{4}$$

where D is a constant for solvent diffusivity, ∇ involves derivatives with respect to the Eulerian coordinates $\boldsymbol{x}$, and c is the true molar concentration per unit physical volume, related to the concentration per unit volume of dry polymer by the relation $c = C/J$. In Lagrangian terms, Eq. (4) can be expressed as

$$\boldsymbol{J} = -\boldsymbol{M}\,\nabla_0\mu, \quad \text{where} \quad M_{KL} = \frac{D}{vkT}(J-1)F^{-1}_{Ki}F^{-1}_{Li}. \tag{5}$$

Replacing this kinetic relation into Eq. (3) and invoking the molecular incompressibility condition, the conservation of solvent molecules can be written as

$$\frac{1}{v}\frac{\partial J}{\partial t} = \nabla_0 \cdot (\boldsymbol{M}\,\nabla_0\mu)\,. \tag{6}$$

Balance of linear momentum, in the absence of external or inertial forces, can be written as

$$\nabla_0 \cdot \boldsymbol{P} = 0, \tag{7}$$

where the $\boldsymbol{P} = \partial W/\partial\boldsymbol{F}$ is the first Piola-Kirchhoff (nominal) stress tensor. Equations (6) and (7) form a system of four coupled and nonlinear partial differential equations, which together with initial and boundary conditions, allow us to solve for the deformation mapping $\boldsymbol{x}(\boldsymbol{X}, t)$ and for the chemical potential $\mu(\boldsymbol{X}, t)$.

The weak form of these equations is the basis of the finite element method.[13] After multiplying Eq. (6) by an arbitrary test function $\eta(\boldsymbol{X})$ compatible with the essential boundary conditions on μ and integrating by parts, conservation of solvent molecules can be written as

$$\int_{\Omega_0} \frac{1}{v}\dot{J}\eta\; dV + \int_{\Omega_0} \nabla_0\eta \cdot (\boldsymbol{M}\,\nabla_0\mu)\; dV = \int_{\Gamma_{N,\mu}} \eta\,\bar{J}_N\; dS \tag{8}$$

where $\dot{(\,)}$ denotes time differentiation, the integrals are performed over the reference configuration, and $\Gamma_{N,\mu}$ is the part of the boundary with prescribed flux $\bar{J}_N$. Balance of linear momentum follows from

$$\int_{\Omega_0} \boldsymbol{P} : \nabla_0\boldsymbol{U}\; dV = \int_{\Gamma_{N,x}} \bar{\boldsymbol{T}} \cdot \boldsymbol{U}\; dS, \tag{9}$$

where $\boldsymbol{U}(\boldsymbol{X})$ is now an arbitrary vector-valued test function, and $\Gamma_{N,x}$ is the part of the boundary with prescribed traction $\bar{\boldsymbol{T}}$.

2. Modeling the gel without epithelial clusters

Our preparation procedure results in partially hydrated PAA gels,[14] which are then bonded to the PDMS substrate and fully hydrated (see Supplementary Fig. 18). We denote the stretch of the partially hydrated gel relative to the reference dry state by λ_p. Upon bonding and full hydration, the gel swells adopting a vertical stretch denoted by λ_{sw}, while upon drying, the vertical stretch is λ_{dry}. Because the gel is bonded to the substrate, the lateral stretch stays at λ_p. See Supplementary Fig. 18 for an illustration.

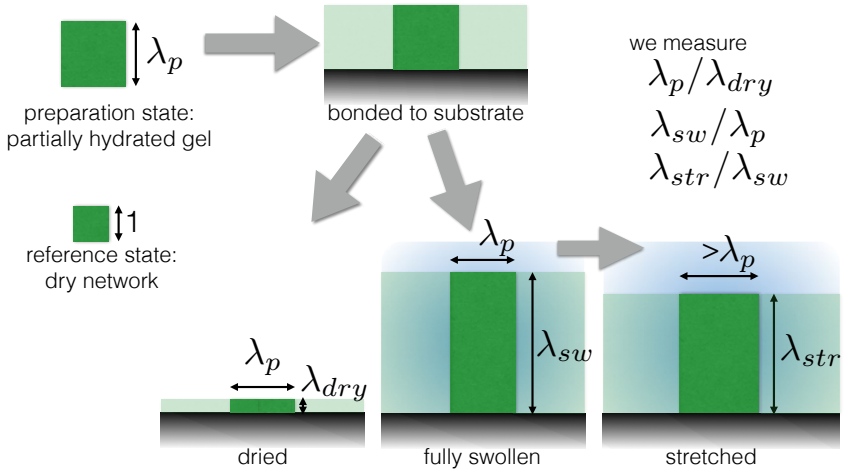

Supplementary Figure 18: Different states of the gel and measurements to fit the material parameters. The green element represents a piece of gel of unit lateral dimensions in the reference dry state. This gel element is first isotropically swollen to adopt a lateral dimension λ_p during preparation. When it is then bonded and fully hydrated, its lateral dimensions are constrained by the substrate and it only swells vertically. Experimentally, we can measure the thickness of the bonded gel relative to the preparation thickness (λ_{sw}/λ_p), the ratio between the dry and the preparation thickness (λ_p/λ_{dry}), and the change in relative thickness under stretch ($\lambda_{str}/\lambda_{sw}$).

The theory presented above allows us to easily characterize uniform states of the gel, for instance when it is in equilibrium with the solvent or upon a sudden stretch. We deal later with more complex situations using finite element simulations. Because of the geometry of the system and the equibiaxial strain applied to the system, the deformation gradient adopts the form

$$\boldsymbol{F} = \begin{bmatrix} \lambda_L & 0 & 0 \\ 0 & \lambda_L & 0 \\ 0 & 0 & \lambda_Z \end{bmatrix}, \tag{10}$$

where λ_L is the lateral stretch relative to the dry state and λ_Z is the stretch in the out-of-plane direction Z. Consequently, $J = \lambda_L^2 \lambda_Z$. In the absence of externally applied forces on the gel surface, mechanical equilibrium along Z is simply $P_{zZ} = 0$, which recalling Eq. (1) can be expressed as

$$0 = NkT\lambda_Z + \frac{1}{\lambda_Z}\left\{-NkT + \frac{kT}{v}\left[J\log\frac{J-1}{J} + 1 + \frac{\chi}{J}\right] - \frac{\mu J}{v}\right\} \tag{11}$$

In the fully swollen and bonded state, $\lambda_L = \lambda_p$ and the gel is in equilibrium with the solvent, i.e. the chemical potential is $\mu = 0$ within the gel. Then, Eq. (11) allows us to compute $\lambda_Z = \lambda_{sw}$ given the properties of the gel N and χ by finding the root of a nonlinear equation.

If the gel is suddenly stretched biaxially to $\lambda_L = \lambda_p(1+\varepsilon)$, where ε denotes the lateral nominal strain, it instantaneously contracts vertically due to incompressibility to adopt a vertical stretch of $\lambda_Z = \lambda_{sw}/(1+\varepsilon)^2$. The chemical potential of the solvent immediately after the sudden stretch can then be computed from Eq. (11), which turns out to be negative if $\varepsilon > 0$. As a result, solvent is driven into the gel, which eventually reaches a new equilibrium vertical stretch denoted by $\lambda_Z = \lambda_{str}$. Again, this stretch can be computed from Eq. (11) imposing $\lambda_L = \lambda_p(1+\varepsilon)$ and $\mu = 0$.

If then the system is suddenly unstretched to $\lambda_L = \lambda_p$, by incompressibility $\lambda_Z = \lambda_{str}(1+\varepsilon)^2$. The excess chemical potential can be computed from Eq. (11), which divided by v can be interpreted as an excess solvent pressure inside of the gel:

$$\Delta p = NkT\frac{\lambda_{str}^2(1+\varepsilon)^4 - 1}{J} + \frac{kT}{v}\left[\log\frac{J-1}{J} + \frac{1}{J} + \frac{\chi}{J^2}\right], \tag{12}$$

where $J = \lambda_p^2\lambda_{str}(1+\varepsilon)^2$. Since the gel is in contact with the solvent, it will progressively deswell to reach $\lambda_Z = \lambda_{sw}$.

Swelling and deswelling are transient processes in which the gel is in a non-uniform state. To obtain $\lambda_Z(Z,t)$ and $\mu(Z,t)$, a system of partial differential equations in one dimension can be easily solved numerically,[7] with zero flux boundary conditions at the bottom, and zero chemical potential and traction at the top. The placement of material positions as a function of time can ben be obtained by integrating $\lambda_Z(Z,t) = \partial z(Z,t)/\partial Z$.

3. Finite element formulation of hydrogel dynamics

Our experimental setup consists of a hydrogel slab bonded to an impermeable substrate, which imposes stretch, and embedded in a solvent. The hydrogel is covered by a pattern of epithelial islands of diameter $2A = 80$ μm, with a typical separation of $2R = 200$ μm. To model the system, we idealize the region around an epithelial cluster as a cylindrical region of gel covered by a disc-like impermeable barrier, see Supplementary Fig. 19.

Due to axisymmetry, we consider the gel domain represented in the right panel of the figure. Because the theory is formulated in a reference dry gel, the dimensions of $\Omega_0 = [0,R_0]\times[0,H_0]$ need to be scaled appropriately to account for swelling and bonding. For instance, for a gel with a swelling stretch of $\lambda_p = 2$, a typical cluster separation of $2R = 200$ μm, and a swollen thickness after bonding H, the dimensions of the reference gel domain should be $R_0 = R/\lambda_p = 50$ μm and $H_0 = H/\lambda_{sw}$. The radius of the impermeable cover in the reference domain should be $A_0 = A/\lambda_p = 20$ μm.

The unknowns of the problem are now $\mu(R,Z,t)$ and the placement of material particles after deformation $r(R,Z,t)$ and $z(R,Z,t)$. The boundary conditions for the problem are as follows. Mechanically, the bottom part of the domain is fully clamped in the partially swollen state, while at the lateral parts of the boundary, only the r component is constrained

$$r(R,0,t) = \lambda_p R, \quad z(R,0,t) = 0, \quad r(0,Z,t) = 0, \quad r(R_0,Z,t) = \lambda_p R_0. \tag{13}$$

All other mechanical boundary conditions are traction-free

$$\bar{T}_z(0,Z,t) = \bar{T}_z(R_0,Z,t) = \bar{T}_r(R,H_0,t) = \bar{T}_z(R,H_0,t) = 0. \tag{14}$$

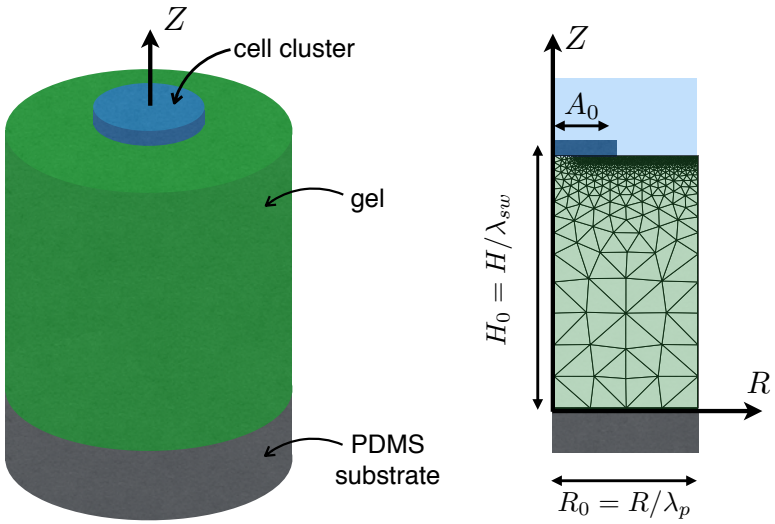

Supplementary Figure 19: Description of the problem setup, axisymmetric domain used in the finite element calculations, and typical finite element mesh.

As for the mass transport boundary conditions, zero flux $\bar{J}_N = 0$ is applied everywhere except in the upper part of the boundary exposed to the solvent, where

$$\mu(R, H_0, t) = 0 \quad \text{for} \;\; A_0 < R < R_0. \tag{15}$$

Placing ourselves immediately after stretch release, when $\lambda_L = \lambda_p$ and $\lambda_Z = \lambda_{str}(1+\varepsilon)^2$, we can compute the excess chemical potential μ^* directly from Eq. (11). Thus, the initial conditions are

$$r(R, Z, 0) = \lambda_p R, \quad z(R, Z, 0) = \lambda_{str}(1+\varepsilon)^2 Z, \quad \mu(R, Z, 0) = \mu^*. \tag{16}$$

Having defined the boundary value problem, we describe next the finite element formulation that we use to approximate the solution numerically. We first summarize the model formulation under axisymmetry. The element of volume is $dV = 2\pi R dR dZ$. Because all fields are independent of the azimuthal angle Θ and there is no azimuthal displacement, $\theta(R, Z, t) = 0$, deformation gradient takes the form

$$\boldsymbol{F} = \begin{bmatrix} \partial r/\partial R & \partial r/\partial Z & 0 \\ \partial z/\partial R & \partial z/\partial Z & 0 \\ 0 & 0 & 1 \end{bmatrix}. \tag{17}$$

We denote by $\tilde{\boldsymbol{F}}$ the upper-left 2×2 submatrix and by $\tilde{J}$ its determinant. Noting that the metric in cylindrical coordinates is not Euclidean, we obtain the following expressions

$$J = \frac{r}{R}\tilde{J}, \quad \text{tr}\left(\boldsymbol{F}^T\boldsymbol{F}\right) = \left(\frac{r}{R}\right)^2 + \text{tr}\left(\tilde{\boldsymbol{F}}^T\tilde{\boldsymbol{F}}\right), \tag{18}$$

which recalling Eq. (1) allow us to evaluate the free energy density.

Denoting by $\tilde{\nabla}_0 = (\partial/\partial R, \partial/\partial Z)$ the nabla operator in the symmetry plane of the reference coordinates, the weak form for balance of linear momentum in the absence of externally applied

tractions takes the form

$$\int_{\Omega_0} \left(\frac{\partial W}{\partial \tilde{\boldsymbol{F}}} : \tilde{\nabla}_0 \boldsymbol{U} + \frac{\partial W}{\partial r} U_r \right) R dR dZ = 0, \tag{19}$$

for any test function $\boldsymbol{U}(R,Z) = (U_r(R,Z), U_z(R,Z))$ consistent with the fixed placement boundary conditions, where

$$\frac{\partial W}{\partial \tilde{\boldsymbol{F}}} = NkT \left(\tilde{\boldsymbol{F}} - \tilde{\boldsymbol{F}}^{-T} \right) + \frac{J}{v} \left[kT f'(J) - \mu \right] \tilde{\boldsymbol{F}}^{-T} \tag{20}$$

and

$$\frac{\partial W}{\partial r} = \frac{1}{r} \left\{ NkT \left[\left(\frac{r}{R} \right)^2 - 1 \right] + \frac{J}{v} \left[kT f'(J) - \mu \right] \right\}. \tag{21}$$

Balance of solvent mass takes the form

$$\int_{\Omega_0} \frac{J}{v} \left(\frac{\dot{r}}{r} + \tilde{\boldsymbol{F}}^{-T} : \dot{\tilde{\boldsymbol{F}}} \right) \eta \, R dR dZ + \int_{\Omega_0} \tilde{\nabla}_0 \eta \cdot \left(\tilde{\boldsymbol{M}} \, \tilde{\nabla}_0 \mu \right) R dR dZ = 0. \tag{22}$$

In the finite element method, the deformation map and the chemical potential are approximated as

$$r(R,Z,t) = \sum_{a=1}^{n} N_a(R,Z) r_a(t), \quad z(R,Z,t) = \sum_{a=1}^{n} N_a(R,Z) z_a(t), \quad \mu(R,Z,t) = \sum_{b=1}^{q} Q_b(R,Z) \mu_b(t), \tag{23}$$

where $N_a(R,Z)$ and $Q_b(R,Z)$ are basis functions supported on a finite element mesh, while $r_a(t)$, $z_a(t)$ and $\mu_b(t)$ are the nodal degrees of freedom. We denote by

$$\mathbf{x}(t) = (r_1(t), z_1(t), r_2(t), z_2(t), \ldots, r_n(t), z_n(t))^T \tag{24}$$

the array containing all the deformation degrees of freedom, so that x_{ai} represents r_a if $i = 1$ and z_a if $i = 2$.

It is very important to choose an appropriate combination of finite element spaces to discretize the deformation and the chemical potential, i.e. the span of the functions $N_a(R,Z)$ and $Q_b(R,Z)$ respectively. Indeed, at short times, this model behaves like an incompressible hyperelastic material, where μ can be interpreted as the pressure.[13] For such problems, the finite element spaces should obey the so-called LBB compatiblity condition.[15] A popular choice of compatible pair adopted here are Taylor-Hood finite elements. We choose $N_a(R,Z)$ as quadratic basis functions and $Q_b(R,Z)$ as linear basis functions supported on a triangulation.

The space-discrete finite element equations can be obtained by plugging Eq. (23) into Eqs. (19) and (22), and representing the variations $(U_r(R,Z), U_z(R,Z))$ and $\eta(R,Z)$ using the basis functions $N_a(R,Z)$ and $Q_b(R,Z)$, respectively. To write them down concisely, we introduce the vector of nodal forces given by

$$\mathrm{f}_{ai} = \frac{kT}{v} \int_{\Omega_0} \left(\left[Nv \left(\tilde{F}_{iI} - \tilde{F}^{-1}_{Ii} \right) + f'(J) J \tilde{F}^{-1}_{Ii} \right] \frac{\partial N_a}{\partial X_I} + \frac{\delta_{i1}}{r} \left\{ Nv \left[\left(\frac{r}{R} \right)^2 - 1 \right] + f'(J) J \right\} N_a \right) R dR dZ, \tag{25}$$

for the $a-$th node along the $i-$th coordinate, and where $i = 1, 2$ correspond to r and z, respectively. Here and elsewhere, we adopt Einstein's summation convention for repeated indices. We also introduce the coupling matrix

$$\mathrm{C}_{bai} = -\int_{\Omega_0} \frac{J}{v}\left(\tilde{F}^{-1}_{Ii}\frac{\partial N_a}{\partial X_I} + \frac{\delta_{i1}}{r}N_a\right) Q_b \, RdRdZ \tag{26}$$

and the diffusion matrix

$$\mathrm{D}_{bc} = \int_{\Omega_0} \frac{D}{vkT}\tilde{F}^{-1}_{Ki}\tilde{F}^{-1}_{Li}\frac{\partial Q_b}{\partial X_K}\frac{\partial Q_c}{\partial X_L} RdRdZ. \tag{27}$$

It should be noted that this vector and these two matrices depend nonlinearly on the finite element deformation given by $\mathbf{x}$.

With these definitions, the discrete finite element equations for balance of linear momentum can be written as

$$0 = \mathrm{f}_{ai}(\mathbf{x}) + \mathrm{C}_{bai}(\mathbf{x})\,\mu_b, \qquad a = 1, \ldots, n, \;\; i = 1, 2, \tag{28}$$

and the discrete equations for solvent mass conservation as

$$\mathrm{C}_{bai}(\mathbf{x})\dot{\mathrm{x}}_{ai} = D_{bc}(\mathbf{x})\,\mu_c, \qquad b = 1, \ldots, q. \tag{29}$$

Because no time-derivatives of μ_b appear, these two sets of equations form a system of differential-algebraic equations to solve for $\mathrm{x}_{ai}(t)$ and $\mu_b(t)$. We developed a Matlab code to implement these finite element equations, which were then integrated in time with a specialized solver (ode15s) for differential-algebraic equations.

4. Finite element calculations

We first consider the conditions of the Control experiments, with a typical gel thickness of $H = 156$ μm and an epithelial island radius of $A = 40$ μm. We later change these dimensions, but not the material parameters. Consequently, the overpressure upon stretch cessation is the same in all cases reported here, $\Delta p \approx 3$ kPa, see Eq. (12). Supplementary Fig. 20a shows selected snapshots of the gel deformation, the solvent flow pattern, and the solvent pressure (μ/v). Starting from an initially uniform solvent over-pressure, the gel starts to relax by solvent efflux at the region of the gel in contact with the external solvent. Because solvent migration couples with the deformation of the gel, the impermeable partial cover produces not only inhomogeneous flow but also inhomogeneous deformation. Within 10 minutes, the gel has nearly equilibrated with the external solvent. The de-swelling of the gel is apparent in the figure.

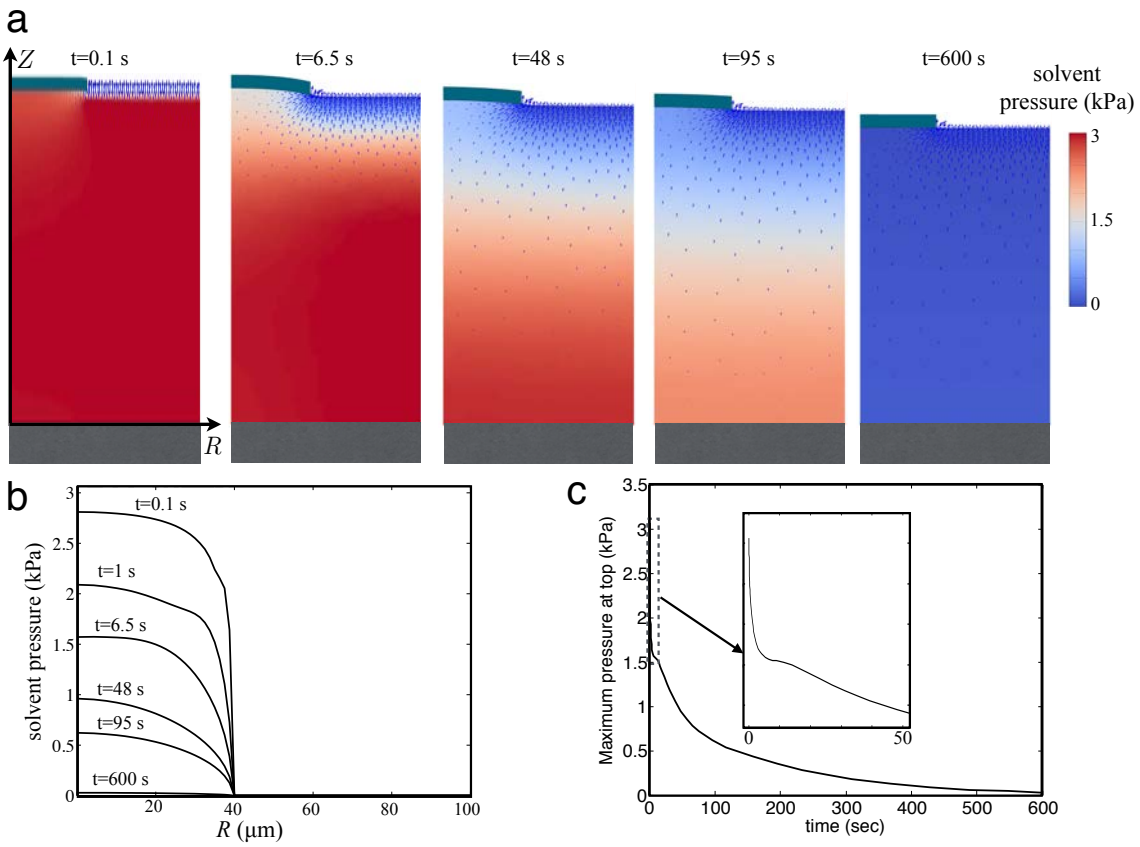

Supplementary Figure 20: Solvent pressure relaxation in the gel. (a) Snapshots of the solvent pressure within the gel (μ/v) at selected instants, plotted on the deformed configuration of the gel. The green region represents the epithelial island, and blue arrows depict the solvent flow pattern. Deformation is not amplified. (b) Solvent overpressure profile in the upper part of the gel at selected instants. (c) Time evolution of the maximum overpressure underneath the epithelial island.

The profiles of the solvent overpressure at the top of the gel for selected instants is shown in Supplementary Fig. 20b. The left part of the domain is covered by an impermeable cover, while the right part is in contact with the bathing solvent. Hydraulic fractures form very early

upon unstretching; they are present as early as we can observe, within seconds of stretch release. At these early times, a strong pressure gradient develops at the boundary of the epithelial island, but is confined to a narrow region only a few microns away from the edge. Consequently, the overpressure is significant (> 1 kPa) throughout most of the island, consistent with the observation that hydraulic fractures form everywhere in the cell clusters (Supplementary Fig. 14).

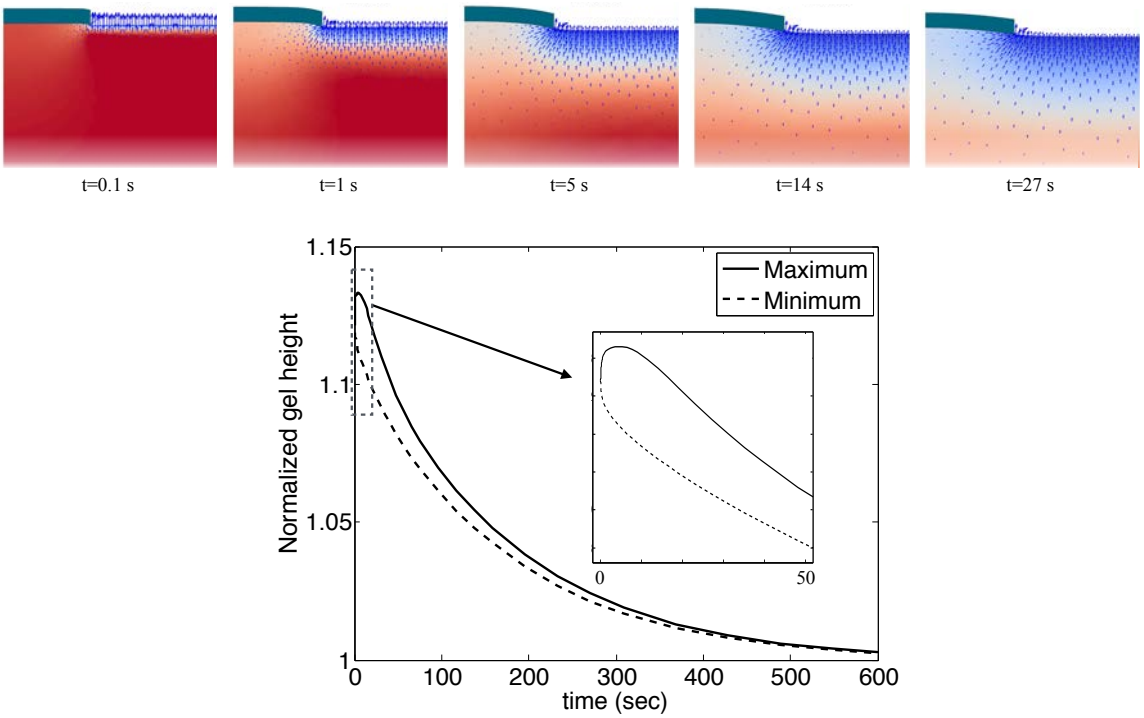

Supplementary Figure 21: Short-time pressure relaxation through deformation of the gel. Selected snapshots of the poroelastic state of the gel at initial stages (top) and time evolution of the maximum and minimum normalized height of the gel top surface.

We expect at least two pressure relaxation times, associated to the lateral dimension of the islands and to the gel thickness. Supplementary Fig. 20c shows that the first of these timescales is of around 1 minute, while the second is about 10 minutes. Interestingly, we observe another very fast relaxation timescale of about 5 seconds. Closely examining the simulations, see Supplementary Fig. 21, we identify that this relaxation mode is genuinely poroelastic, and not merely diffusive. Indeed, underneath the impermeable cover, the solvent overpressure drives elastic deformation of the gel. The fast pressure relief mechanism (see inset in Supplementary Fig. 20c) can be directly linked to local and transient bulging of the gel (see inset in Supplementary Fig. 21).

We turn now to the effect of the thickness of the gel. We compare the response of the Control gel with that of a Thick gel (H = 336 μm) and a Thin gel (H = 62 μm). In the absence of epithelial islands, we expect the gel poromechanics to be independent of gel thickness at initial stages, when the presence of the lower boundary is not felt, while at later stages, the relaxation time should scale with H^2 (see Supplementary Note 2). Supplementary Fig. 22 shows that the long-time behavior conforms with this expectation, with the Thin gel fully relaxing within 2

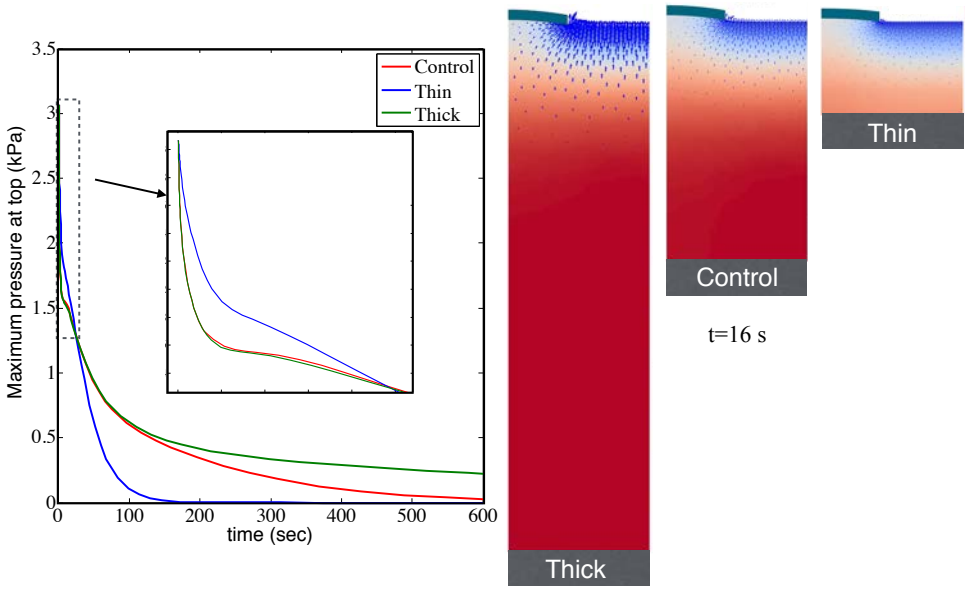

Supplementary Figure 22: Effect of gel thickness on pressure relaxation.

minutes, and the Thick gel being still far from equilibration after 10 minutes. However, at short times, the pressure relaxation of the Thin gel is significantly slower than that of the the Control and Thick gels. Again, the explanation of this discrepancy lies in the fast poroelastic mechanism alluded to previously. For the Thin gel, bonding to the substrate imposes a stronger mechanical constraint, which impairs the localized bulging underneath the epithelium.

Supplementary Fig. 23 compares the Control setup with another geometry with a larger island ($A = 100$ μm). The larger island leads to a significantly slower relaxation associated with the lateral equilibration, which becomes here comparable to the vertical equilibration. Furthermore, upwards bulging occurs only near the rim of the epithelial island, and is less effective in lowering the solvent pressure for the larger island.

Finally, in these finite element calculations, we have assumed that the epithelial island is impermeable. However, our data suggests that, because of the solvent overpressure, hydraulic fractures open, which contain part of the solvent expelled by the gel. This transient and limited permeability of the epithelium should further reduce the solvent pressure underneath the island. To estimate the strength of this effect, we introduce an upwards solvent flux consistent with the time-scale of fracture opening (a few seconds) and with the measured volume within the fractures per unit area of epithelium (0.35 μm). Supplementary Fig. 24 shows that indeed this mechanism reduced the solvent pressure underneath the gel, but the effect is not very significant in magnitude or duration.

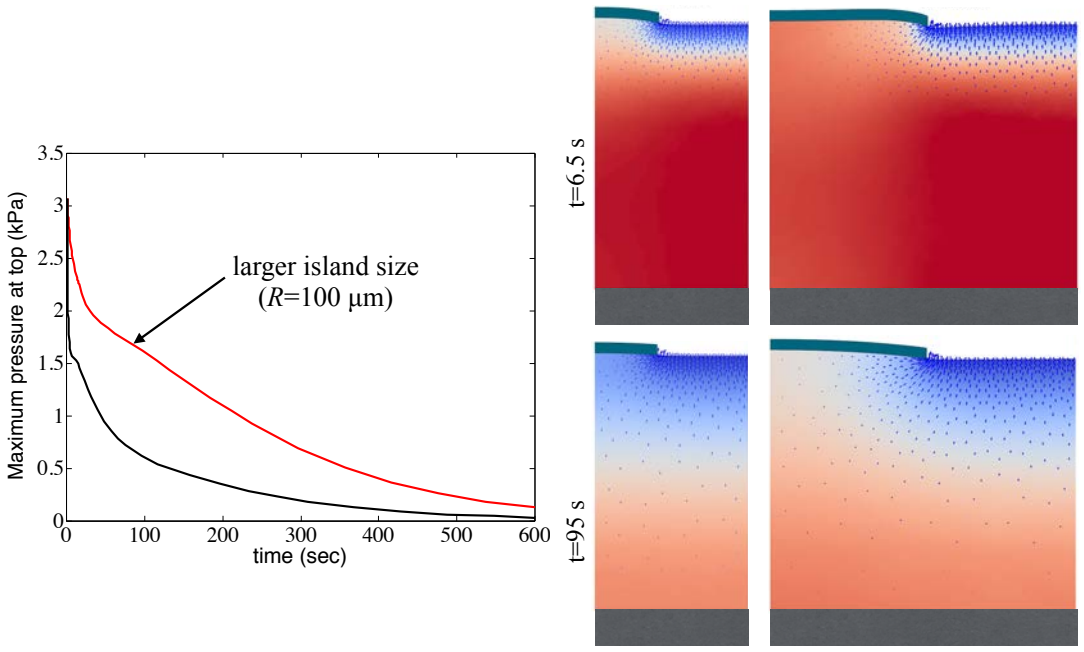

Supplementary Figure 23: Slower pressure relaxation of a larger epithelial island, compared to the control island.

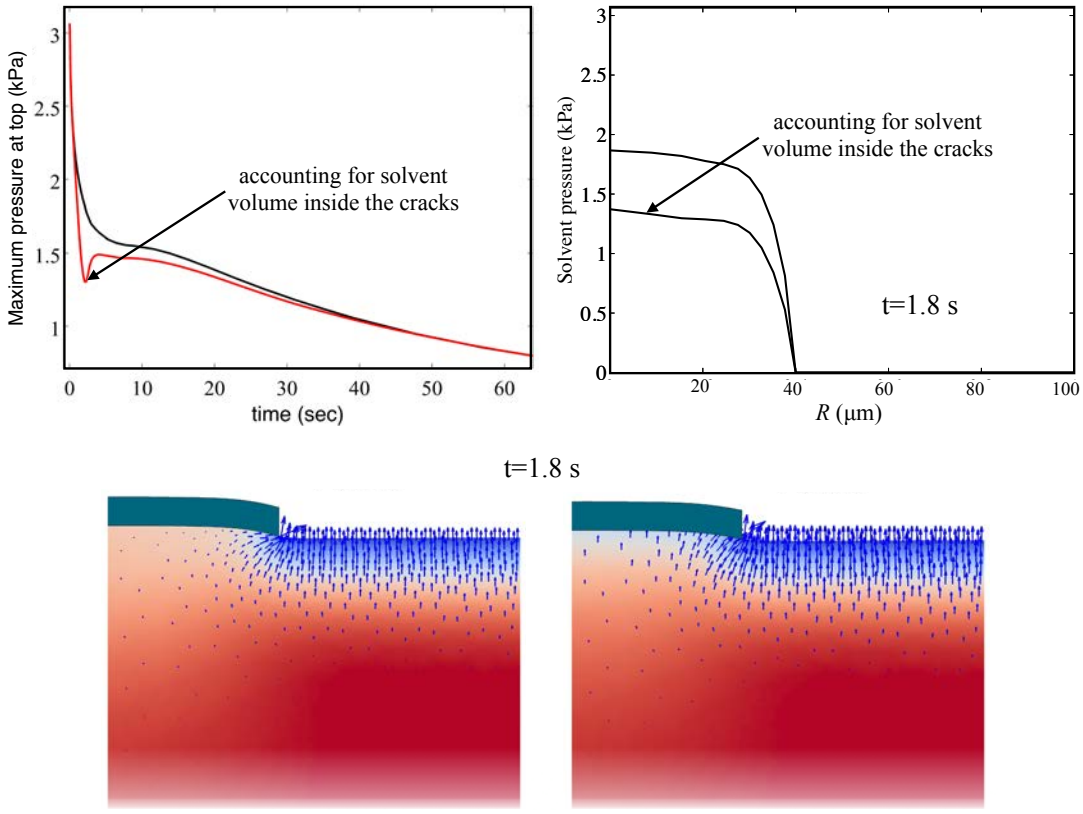

Supplementary Figure 24: Pressure relaxation due to flow of solvent into the epithelial fractures. We compare a simulation with an impermeable epithelium ($\bar{J} = 0$) to a simulation with $\bar{J}$ accounting for the transient efflux of solvent from the gel into the hydraulic fractures. The lower-right snapshot exhibits a non-zero solvent flux through the epithelium, contrary to the case of an impermeable barrier as in the lower-left snapshot.

Supplementary Note 2: PAA hydrogel behavior

1. Fitting model parameters

We denote the thickness of the bonded and fully hydrated gel by H. To test if our PAA gels conform to the theory presented above, we considered a set of gels of identical preparation but different thickness, which we subjected to the stretch/unstretch maneuver (see Fig. 4 in main text) in the absence of a covering impermeable barrier (epithelium). The poroelastic flows caused by stretching, which induce a time-dependent evolution of the gel thickness $h(t)$ and volume, relax at much longer time-scales for thicker gels. According to the theory or poroelasticity, the swelling/de-swelling dynamics of these gels with different thickness should collapse if we plot the normalized gel thickness $h(t)/H$ against $\sqrt{t}/H$.[8,7] Supplementary Fig. 25 shows that this is the case for all our data.

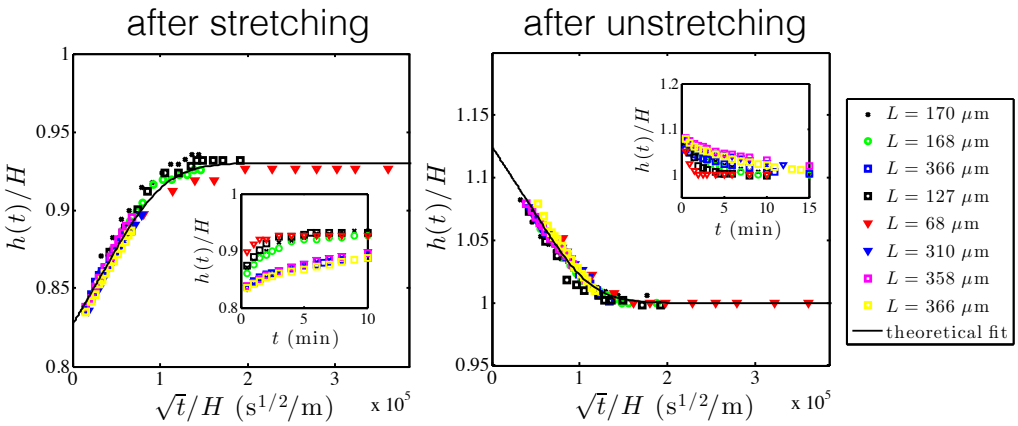

Supplementary Figure 25: Swelling and de-swelling of PAA gels of different thicknesses. The insets show the normalized height as a function of time. When properly normalized, the behavior of all gels collapses into a single response, well described by the theory (solid line).

We then tried to fit the model parameters to our data for three different gel preparations, which we refer to as Control, Stiff and Soft. As illustrated in Supplementary Fig. 18, the gel is prepared in a partially hydrated state, whose stretch λ_p relative to the reference dry state is not known. Therefore, the parameters we need to fit are λ_p, N, χ, and the kinetic parameter D. The three stretch ratios shown in the figure were measured experimentally for several gels. Since these three stretch ratios can be computed from the model as described in Supplementary Note 1 given N, λ_p and χ, they provide a way to fit these parameters.

Young's modulus Y_p at the preparation state is determined approximately by the polymerization protocol.[14] The nominal values for Y_p in the Control, Stiff and Soft gels are 12 kPa, 200 kPa and 0.2 kPa. Theoretically, in the regime of fast deformations (no time for solvent migration) at the preparation state, it is given by $Y_p = 3NkT/\lambda_p$.[16] This provides extra information to fit the material parameters.

D was fitted from the kinetics of gel height evolution upon stretching, e.g. as shown in Supplementary Fig. 25. For this, we solved numerically for $\lambda_Z(Z,t)$ and $\mu(Z,t)$ as described in Supplementary Note 1, and then integrated in space $\lambda_Z(Z,t)$ to obtain $h(t)$.

Supplementary Table 1: Material parameters

	Nv	Y_p (kPa)	χ	λ_p	D (m^2/s)
Control	$2 \cdot 10^{-4}$	12	0.46	2	$1{\cdot}10^{-7}$
Stiff	$2.7 \cdot 10^{-3}$	202	0.4	1.6	$6{\cdot}10^{-9}$
Soft	$4.5 \cdot 10^{-6}$	0.2	0.485	2.6	$1{\cdot}10^{-6}$

The parameters shown in Supplementary Table 1 are consistent with measurements from three samples for each gel stiffness. While our parameter fitting procedure leaves room for some ambiguity, we checked that the overpressure generated upon unstretching is quite insensitive to the precise combination of parameters consistent with the measurements. Note that the diffusivity D reported here is related but does not coincide with the effective diffusivity measured in some experiments using linear poroelasticity,[16] which depends on the swelling state of the material and is generally much smaller. The solid line in Supplementary Fig. 25 represents the model prediction for the swelling/de-swelling dynamics, showing very good agreement with the experimental data.

2. Solvent efflux and overpressure

Having tested that our PAA gels conform well to the theory of ideal hydrogels, we turn to predictions of the model. The model predicts that the swelling/de-swelling dynamics of the supported gel upon sudden stretch/unstretch follow

$$\frac{h(t)}{H} = g\left(\frac{\sqrt{Dt}}{H}; N, \chi, \lambda_p\right), \tag{30}$$

for some function g that depends only on the chemistry and preparation of the gel through the parameters χ, N, and λ_p. Time-differentiating this expression, we obtain the fluid velocity at the free-surface of the gel

$$v_{top} = h'(t) = \frac{1}{2}\sqrt{\frac{D}{t}}g'\left(\frac{\sqrt{Dt}}{H}; N, \chi, \lambda_p\right). \tag{31}$$

As shown in Supplementary Fig. 26, before the effect of the bottom boundary is felt, i.e. for small t relative to H^2/D, g' is nearly constant. Thus, the flow rate at the top of the gel does not depend on gel thickness at the initial stages. Note also that the flow rate is singular (infinite) at $t = 0^+$. At later stages, there is a thickness-dependent cross-over time at which flow gradually ceases. Focusing on the Control gel, the cross-over time is about 4 min for $H = 150$ μm, 0.6 min for $H = 60$ μm, and 20 min for $H = 350$ μm.

Upon unstretching and assuming that the hydrogel is covered by an impermeable barrier (the epithelium), solvent migration is not possible and the model allows us to calculate the resulting overpressure beneath the barrier from Eq. (11). For the Control gel and a stretch magnitude of 10%, we find $\Delta p = 3$ kPa. For the Stiff gel, the overpressure is significantly higher, $\Delta p = 44$ kPa, while for the Soft gel we find $\Delta p = 0.08$ kPa. We also estimate the overpressure for the Control gel and a stretch magnitude of 5% as 1.6 kPa, and for a stretch magnitude of 15% as 4.4 kPa.

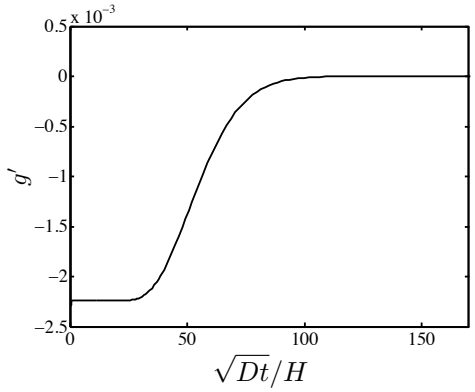

Supplementary Figure 26: Nondimensional function governing the solvent efflux.

In our interpretation of the experiments, we view the epithelium as an impermeable barrier. However, the plasma membrane has finite permeability,[17] in the order of $P_f = 0.01$ cm/s for the basolateral membrane of kidney cells.[18] Consequently, the overpressure upon stretch cessation could be relieved by water permeation through the plasma membrane. We argue next that this competing mechanism is very small compared to pressure relief by opening hydraulic fractures.

In the experiments with the Control gel, the typical volume enclosed within the fractures is of about 60 μm^3 per cell for a cell of lateral dimension $L = 15$ μm. These fractures are observed very early after stretch cessation, within seconds. We estimate next the volume of water that would cross the basal membrane of a cell in $T = 2$ seconds by permeation through the membrane. The water flux follows $J_v = k_m \Delta p$, where $k_m = P_f v/KT \approx 10^{-12}$ m^3/(Ns) and $\Delta p \approx 3$ kPa. Thus, the water volume by permeation per cell is $J_v L^2 T \approx 1.3$ μm^3, much smaller than the volume within the hydraulic fractures. Furthermore, this is an overestimation of the volume of water crossing the epithelium by permeation through the transcellular pathway, since Δp rapidly drops as shown by the simulations.

3. Ideal elastomeric hydrogel vs. physiological ECM

The physiological extracellular matrix adjacent to an epithelial layer exhibits broad chemical diversity and spatial heterogeneity, and is composed of cross-linked protein filaments (collagen, fibronectin, elastin) embedded in a swollen hydrogel of glycan polymer chains.[19] It can therefore be viewed as a complex mixture of two components: a network of semi-flexible polymers, and an elastomeric hydrogel. As a result, the theory of poroelasticity outlined above will not properly capture specific types of matrix dominated by the semi-flexible component. In these networks, rather than chain and mixing entropy, the behavior is dominated by filament bending, resulting in unusual and fundamentally nonlinear mechanical properties such as a large negative normal stress under simple shear.[20] Interestingly, under biaxial stretch in similar conditions to ours, filament aligning and buckling has been shown to lead to an extreme volumetric behavior under large lateral stretches contrary to the one reported here: collagen gels expel fluid during severe stretching rather than during stretch release.[21] Our experiments show that the volumetric behavior of some physiological matrix compositions, including Matrigel and decellularized porcine matrix, is very similar to that of polyacrylamide gels, suggesting that the ideal hydrogel behavior, and not semi-flexible network behavior, is dominant.

Supplementary Note 3: Estimation of the work of cell-cell separation

Our observations provide a rough quantification of the work of cell-cell separation Γ. Ignoring dissipative mechanisms within the gel or the cells and ignoring cell-matrix decohesion, we assume that the work provided by the hydrostatic pressure Δp when opening gaps of volume V is spent in fracturing the cell-cell contacts of area A and in increasing the cortex area by δS

$$\Delta p V = \Gamma A + T \delta S, \tag{32}$$

where T is the cortical tension (see Charras et al.[22] for a related calculation). Since the size of the gaps does not depend significantly on cortex contractility (see Fig. 5 of main text), we neglect the work of cortical tension in our calculation. The examination of z-stacks provides an estimation of the volume to fractured area ratio in individual gaps or in the whole pattern. In either case, we obtain $V/A \approx 2$ μm. Since $\Delta p \approx 3$ kPa, we estimate $\Gamma \approx 6$ mN/m. This figure for the work of separation, which should not be confused with the adhesion surface tension,[23] is about an order of magnitude smaller than that estimated in tensile fracturing essays on suspended monolayers.[24]

Supplementary References

[1] Ostuni, E., Kane, R. S., Chen, C. S., Ingber, D. E., and Whitesides, G. M. Patterning mammalian cells using elastomeric membranes. *Langmuir*, 16:7811–7819, 2000.

[2] Poujade, M., Grasland-Mongrain, E., Hertzog, A., Jouanneau, J., Chavrier, P., Ladoux, B., Buguin, A., and Silberzan, P. Collective migration of an epithelial monolayer in response to a model wound. *Proc. Natl. Acad. Sci. U. S. A.*, 104:15988–15993, 2007.

[3] Serra-Picamal, X., Conte, V., Vincent, R., Anon, E., Tambe, D. T., Bazellieres, E., Butler, J. P., Fredberg, J. J., and Trepat, X. Mechanical waves during tissue expansion. *Nat. Phys.*, 8:628–634, 2012.

[4] Mertz, A., Banerjee, S., Che, Y., German, G., Xu, Y., Hyland, C., Marchetti, M., Horsley, V., and Dufresne, E. Scaling of traction forces with the size of cohesive cell colonies. *Phys. Rev. Lett.*, 108:198101, 2012.

[5] Mertz, A. F., Che, Y., Banerjee, S., Goldstein, J. M., Rosowski, K. A., Revilla, S. F., Niessen, C. M., Marchetti, M. C., Dufresne, E. R., and Horsley, V. Cadherin-based intercellular adhesions organize epithelial cell–matrix traction forces. *Proc. Natl. Acad. Sci. U. S. A.*, 110:842–847, 2013.

[6] Vedula, S. R. K., Hirata, H., Nai, M. H., Brugués, A., Toyama, Y., Trepat, X., Lim, C. T., and Ladoux, B. Epithelial bridges maintain tissue integrity during collective cell migration. *Nat. Mater.*, 13:87–96, 2014.

[7] Hong, W., Zhao, X., Zhou, J., and Suo, Z. A theory of coupled diffusion and large deformation in polymeric gels. *J. Mech. Phys. Solids*, 56:1779–1793, 2008.

[8] Yoon, J., Cai, S., Suo, Z., and Hayward, R. C. Poroelastic swelling kinetics of thin hydrogel layers: comparison of theory and experiment. *Soft Matter*, 6:6004, 2010.

[9] Li, J., Hu, Y., Vlassak, J. J., and Suo, Z. Experimental determination of equations of state for ideal elastomeric gels. *Soft Matter*, 8:8121, 2012.

[10] Hong, W., Zhao, X., and Suo, Z. Large deformation and electrochemistry of polyelectrolyte gels. *J. Mech. Phys. Solids*, 58:558–577, 2010.

[11] Hooper, H. H., Baker, J. P., Blanch, H. W., and Prausnitz, J. M. Swelling equilibria for positively ionized polyacrylamide hydrogels. *Macromolecules*, 23:1096–1104, 1990.

[12] Hong, W., Liu, Z., and Suo, Z. Inhomogeneous swelling of a gel in equilibrium with a solvent and mechanical load. *Int. J. Solids Struct.*, 46:3282–3289, 2009.

[13] Belytschko, T., Liu, W., and Moran, B. *Nonlinear finite elements for continua and structures*. Wiley, 2000.

[14] Yeung, T., Georges, P. C., Flanagan, L. a., Marg, B., Ortiz, M., Funaki, M., Zahir, N., Ming, W., Weaver, V., and Janmey, P. a. Effects of substrate stiffness on cell morphology, cytoskeletal structure, and adhesion. *Cell Motil. Cytoskeleton*, 60:24–34, 2005.

[15] Girault, V. and Raviart, P. A. *Finite Element Methods for Navier–Stokes Equations*. Springer-Verlag, Berlin, 1986.

[16] Bouklas, N. and Huang, R. Swelling kinetics of polymer gels: comparison of linear and nonlinear theories. *Soft Matter*, 8:8194, 2012.

[17] Verkman, A. Water Permeability Measurement in Living Cells and Complex Tissues. *J. Membr. Biol.*, 87:73–87, 2000.

[18] Verkman, A. and Ives, H. Water permeability and fluidity of renal basolateral membranes. *Am. J. Physiol. . . .*, 250:F633–F643, 1986.

[19] Frantz, C., Stewart, K. M., and Weaver, V. M. The extracellular matrix at a glance. *J. Cell Sci.*, 123:4195–200, 2010.

[20] Janmey, P. a., McCormick, M. E., Rammensee, S., Leight, J. L., Georges, P. C., and MacKintosh, F. C. Negative normal stress in semiflexible biopolymer gels. *Nat. Mater.*, 6:48–51, 2007.

[21] Vader, D., Kabla, A., Weitz, D., and Mahadevan, L. Strain-induced alignment in collagen gels. *PLoS One*, 4:e5902, 2009.

[22] Charras, G. T., Yarrow, J. C., Horton, M. a., Mahadevan, L., and Mitchison, T. J. Non-equilibration of hydrostatic pressure in blebbing cells. *Nature*, 435:365–9, 2005.

[23] Maître, J.-L. and Heisenberg, C.-P. Three functions of cadherins in cell adhesion. *Curr. Biol.*, 23:R626–33, 2013.

[24] Harris, A. R., Peter, L., Bellis, J., Baum, B., Kabla, A. J., and Charras, G. T. Characterizing the mechanics of cultured cell monolayers. *Proc. Natl. Acad. Sci. U. S. A.*, 109: 16449–54, 2012.